SCIENTIFIC REPORTS

OPEN

SUBJECT AREAS:
STRUCTURE OF SOLIDS AND LIQUIDS
TOPOLOGICAL INSULATORS
METALS AND ALLOYS
PHASE TRANSITIONS AND CRITICAL PHENOMENA

Received
3 June 2013

Accepted
29 August 2013

Published
18 September 2013

Correspondence and requests for materials should be addressed to Y.W. (ywang235@oakland.edu)

Sb_2Se_3 under pressure

Ilias Efthimiopoulos[1], Jiaming Zhang[2], Melvin Kucway[1], Changyong Park[3], Rodney C. Ewing[2] & Yuejian Wang[1]

[1]Department of Physics, Oakland University, Rochester, MI, 48309, [2]Departments of Earth & Environment Science and Materials Science & Engineering, University of Michigan, Ann Arbor, MI, 48109, [3]High Pressure Collaborative Access Team, Geophysical Laboratory, Carnegie Institution of Washington, Argonne, IL 60439.

Selected members of the A_2B_3 (A = Sb, Bi; B = Se, Te) family are topological insulators. The Sb_2Se_3 compound does not exhibit any topological properties at ambient conditions; a recent high-pressure study, however, indicated that pressure transforms Sb_2Se_3 from a band insulator into a topological insulator above ~2 GPa; in addition, three structural transitions were proposed to occur up to 25 GPa. Partly motivated by these results, we have performed x-ray diffraction and Raman spectroscopy investigations on Sb_2Se_3 under pressure up to 65 GPa. We have identified only one reversible structural transition: the initial *Pnma* structure transforms into a disordered cubic bcc alloy above 51 GPa. On the other hand, our high-pressure Raman study did not reproduce the previous results; we attribute the discrepancies to the effects of the different pressure transmitting media used in the high-pressure experiments. We discuss the structural behavior of Sb_2Se_3 within the A_2B_3 (A = Sb, Bi; B = Se, Te) series.

The A_2B_3 (A = Sb, Bi; B = S, Se, Te) series consists of layered chalcogenide semiconductors that have attracted considerable interest, mainly due to their exceptional thermoelectric properties[1]. More recently, three members of this series, namely the Bi_2Te_3, Sb_2Te_3, and Bi_2Se_3 compounds, were shown to exhibit topological properties[2,3]. This discovery has revitalized the scientific interest in these materials[4,5].

At ambient conditions, the A_2B_3 (A = Sb, Bi; B = S, Se, Te) family is divided into two structural classes: the heavier Bi_2Se_3, Bi_2Te_3, and Sb_2Te_3 compounds adopt a rhombohedral structure (SG *R*-3*m*, *Z* = 3), which is composed of layers of AB_6 octahedra stacked perpendicular to the long *c*-axis[6]; the lighter Bi_2S_3, Sb_2S_3, and Sb_2Se_3 materials on the other hand, crystallize in an orthorhombic phase (SG *Pnma*, *Z* = 4, U_2S_3-type), made up of AB_7 and AB_{7+1} polyhedra (**Fig. 1** and Supplementary **Fig. S1** online).

Pressure provides a means for "tuning" the physical properties of these compounds. As an example, their thermoelectric properties are enhanced by application of external pressure[1], a feature attributed to an electronic topological transition. More recent and detailed high-pressure investigations on Bi_2Te_3[6–13], Bi_2Se_3[14–18], and Sb_2Te_3[9,19–23] have revealed a plethora of phase transitions. In particular, novel structures with higher cationic coordinations[6,7,14,15,18–21], insulator-to-metal transitions[9,16], and even superconductivity[8,12,13,23] have been observed upon increasing pressure. Quite surprisingly, the compounds crystallizing in the *R*-3*m* structure do not adopt the denser *Pnma* phase upon compression. The only known exception is Bi_2Se_3, which can adopt the *Pnma* structure at combined high-pressure and high-temperature conditions[24] or, as recently shown, at ambient conditions after high-pressure treatment[15].

The present study focuses on the effect of pressure on the structural and vibrational properties of Sb_2Se_3, which is an insulator with a ~1 eV band gap[25]. Even though it does not exhibit the topological properties of the Sb_2Te_3, Bi_2Te_3, and Bi_2Se_3 compounds, Sb_2Se_3 has attracted significant interest over the years as a potential candidate for optical storage devices[26], as well as in photovoltaic[27] and thermoelectric[28] applications. Two recent studies on Sb_2Se_3[29,30] indicated the possibility of a pressure-induced electronic topological transition, thus transforming the material from a normal band insulator into a topological insulator upon pressure application. These investigations, however, considered the *R*-3*m* structure (isostructural to Bi_2Te_3) as an ambient-pressure phase for Sb_2Se_3, a modification which has not been observed experimentally. In addition, a most recent high-pressure Raman study on Sb_2Se_3 indicated several phase transitions taking place up to ~25 GPa[29]. Therefore, a detailed structural investigation of Sb_2Se_3 is necessary in order to clarify any potential pressure-induced phase transitions. The key findings of this work can be summarized as follows:

(I) A novel binary alloy between Sb and Se atoms was observed. In particular, the ambient-pressure *Pnma* phase of Sb_2Se_3 persists up to ~51 GPa; beyond that pressure, Sb_2Se_3 begins to transform into a disordered cubic bcc phase (SG *Im*-3*m*, *Z* = 2), similar to the Bi_2Te_3[6,7] and Sb_2Te_3[19,20] compounds. The transition, which is reversible, is not fully completed up to the highest pressure reached here, i.e. 65 GPa.

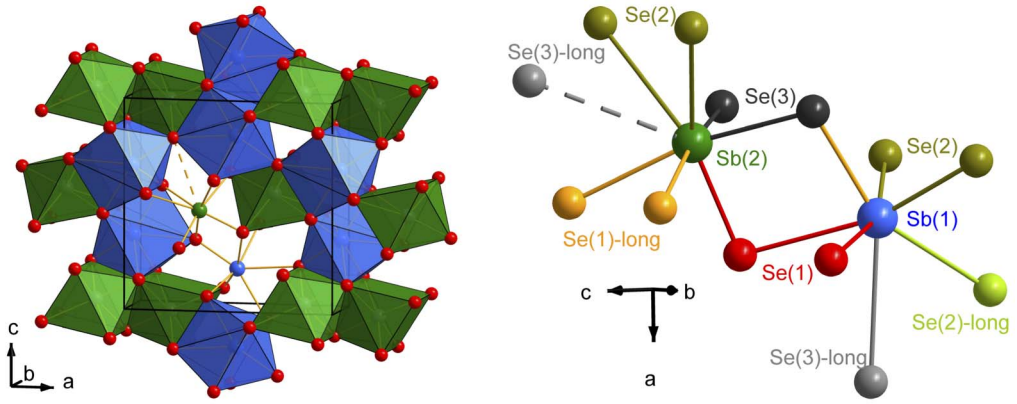

Figure 1 | (Left) The unit cell of Sb_2Se_3 at ambient conditions (SG *Pnma*, $Z = 4$). The blue, green, and red spheres correspond to Sb(1), Sb(2), and Se ions, respectively. The Sb(1)Se_7 (blue) and Sb(2)Se_{7+1} (green) polyhedra are also displayed. (Right) Sketch of the coordination environment around the Sb(1) and Sb(2) cations. The various Sb-Se bonds are depicted by different colors.

(II) To our knowledge, a direct structural transition from the *Pnma* phase into any other structure type has not previously been observed for any A_2B_3 materials. Therefore, this study adds a new structural "path" to the *P-T* phase diagrams of A_2B_3 compounds.

(III) The high-pressure Raman study on Sb_2Se_3 could not reproduce the recently reported results[29]. This discrepancy prompted a more detailed investigation of the Raman response of Sb_2Se_3 from our side, under both ambient- and high-pressure conditions. Considering the available literature, we offer a thorough discussion on the vibrational properties of Sb_2Se_3.

Results

At ambient conditions, Sb_2Se_3 adopts an orthorhombic *Pnma* structure (U_2S_3-type, **Fig. 1**). There are two non-equivalent Sb cation sites in this phase, denoted as Sb(1) and Sb(2) in **Fig. 1**. The Sb(1) cation is coordinated by seven Se anions; on the other hand, the coordination around the Sb(2) site can be described as of (7 + 1) with respect to the Se ions. A more detailed description of the *Pnma* structure is provided in the Supplementary Information online.

Overall, Sb_2Se_3 undergoes one structural transition under pressure (**Fig. 2**): the initial *Pnma* phase begins to transform into a disordered bcc structure (SG *Im*-3*m*, $Z = 2$) above 51 GPa. The transition to the bcc phase is almost completed at 65 GPa. Upon pressure release, the bcc phase persists down to 35 GPa; below that pressure, Sb_2Se_3 reverts to the ambient-pressure *Pnma* phase (see Supplementary **Fig. S2** online). In the recovered sample, the XRD peaks are significantly broadened (bottom XRD pattern in Supplementary **Fig. S2** online), thus hindering any reliable refinement. The reversibility of the ambient-pressure *Pnma* structure is verified by our Transmission Electron Microscopy (TEM) study on the recovered Sb_2Se_3 sample (see Supplementary **Figs. S4&S5** online).

For the initial *Pnma* phase, Rietveld refinements were possible up to ~35 GPa; both the unit cell constants, as well as the interatomic parameter evolution as a function pressure could be obtained (**Fig. 3**). An example of a refined XRD pattern is displayed in **Fig. 2(b)**, whereas the extracted crystallographic parameters are listed in **Table 1**. The Bragg peaks corresponding to the *Pnma* phase broaden significantly above 40 GPa [**Fig. 2(a)**]; therefore, only the lattice parameters could be obtained beyond that pressure.

The pressure dependence of the lattice parameters for the *Pnma* structure is plotted in **Fig. 3(a)**. The long orthorhombic *a*- and *c*-axes, which lie very close in values throughout the investigated pressure range, exhibit a similar non-linear pressure-induced behavior, with a change in their slopes at about 20 GPa. We should note here that a structural transition has been claimed to take place at about 20 GPa for Sb_2Se_3 from a recent Raman investigation[29]. Since we do not detect any changes in our XRD patterns, and considering that our Raman spectra do not reproduce the pressure-induced Raman response of Sb_2Se_3 reported in Ref. 29 as we discuss in more detail below, we attribute this change in the pressure dependence of both the *a*- and *c*-axes to a decrease in the compressibility of Sb_2Se_3 along these two directions beyond 20 GPa. On the other hand, the short *b*-axis exhibits an almost linear (within error) pressure-change up to 48 GPa.

The *P-V* data for the *Pnma* phase of Sb_2Se_3 are shown in **Fig. 3(b)**. By employing the measured zero-pressure volume per formula unit $V_0/Z = 136.4$ Å^3, the Birch-Murnaghan EOS fitting yields a bulk modulus $B_0 = 30(\pm 1)$ GPa and its pressure derivative $B'_0 = 6.1(\pm 0.2)$. The obtained B_0 and B'_0 values are consistent with those of isostructural Sb_2S_3[31] and Bi_2S_3[32] compounds.

The effect of pressure on the interatomic Sb-Se bond lengths for both Sb(1) and Sb(2) cations within the Sb(1)Se_7 and Sb(2)Se_{7+1} polyhedral cages is displayed in **Figs. 3(c,d)**. In the low-pressure regime, the Se-coordination environment around both Sb(1) and Sb(2) cations is highly asymmetric, as indicated by the large dispersion of the Sb-Se bond length values within the respective polyhedra. The effect of pressure is more pronounced for the longer Sb-Se bonds; the shorter Sb-Se bonds on the other hand, remain almost unaffected upon increasing pressure [**Figs. 3 (c, d)**]. The second observation is that pressure "forces" the various Sb-Se bond lengths of the Sb(1)Se_7 polyhedra to adopt similar values at ~35 GPa [**Fig. 3(d)**]. This effect can be translated into a pressure-induced "symmetrization" of the Sb(1)Se_7 polyhedral units. Actually, the distortions of the coordination polyhedra around the Sb^{3+} cations reflect the stereochemical activity of the lone electron pairs of Sb^{3+}, as discussed in more detail in the Supplementary Information.

Above 51 GPa, new Bragg peaks appear in the XRD patterns at about 11°, 15°, and 19° (**Fig. 2**). Upon further pressure increase, these new peaks gain in intensity, indicative of a pressure-induced structural transition. The high-pressure phase can be assigned to a simple, yet disordered, bcc structure (*Im*-3*m*, $Z = 2$). Within the *Im*-3*m* phase, the Sb and Se atoms are randomly distributed on the bcc lattice sites, forming a Sb-Se substitutional alloy. A similar phase transition has been observed for the Bi_2Te_3[6,7] and Sb_2Te_3[19,20] compounds above ~15 GPa and ~22 GPa, respectively.

The only high-pressure studies conducted on U_2S_3-type compounds up to now are those on Sb_2S_3[31] and Bi_2S_3[32] up to 10 GPa, and on the Bi_2Se_3-II phase up to 26 GPa[15]. In all of these studies, no structural transition was observed under pressure. Therefore, a *direct* pressure-induced structural transition from the U_2S_3-type phase to another structure type (*Im*-3*m*) has been observed here for the first

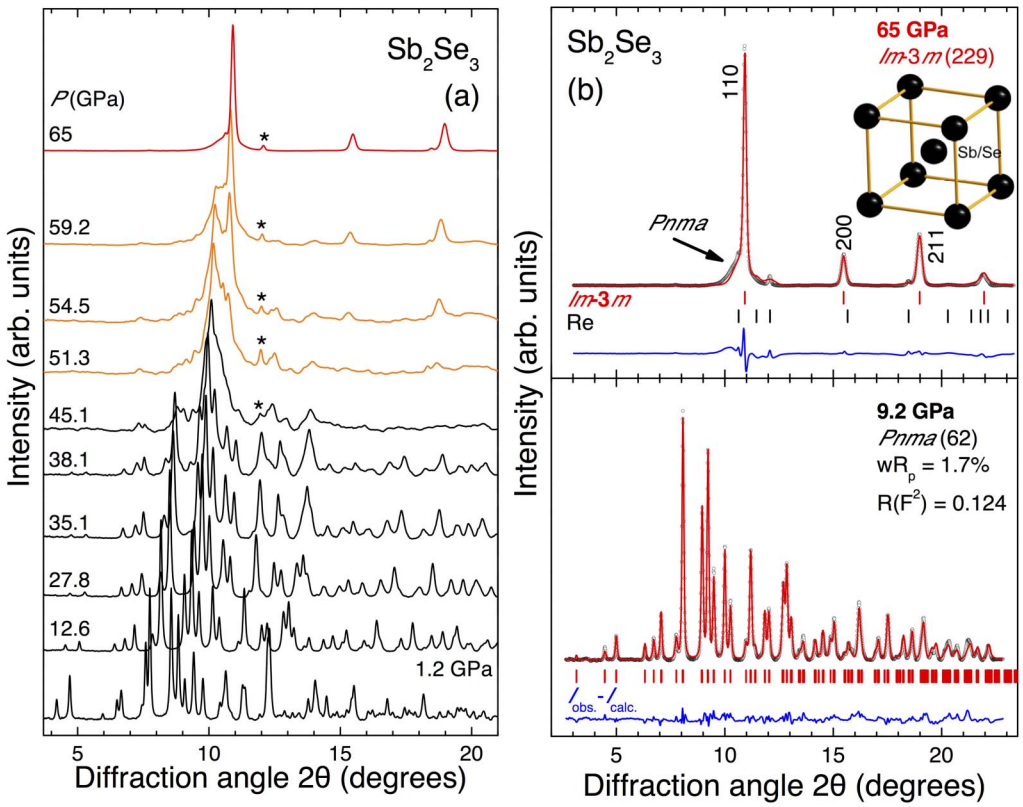

Figure 2 | (a) XRD patterns of Sb_2Se_3 at selected pressures ($T = 300$ K, $\lambda = 0.4246$ Å). The various phases are indicated by different colors: black for the starting *Pnma* structure, red for the high-pressure *Im*-3*m* modification, and orange for the coexistence regime. Asterisks mark the strongest Bragg peak of the rhenium gasket. Background has been subtracted for clarity. (b) Refined XRD patterns of Sb_2Se_3 at 9.2 GPa (*Pnma*, bottom) and at 65 GPa (*Im*-3*m*, top). Dots correspond to the measured spectra and the red solid lines represent the best refinements. The difference spectra between the measured and the refined patterns are depicted too (blue lines). Vertical ticks mark the Bragg peak positions.

time in the case of Sb_2Se_3. This result supplements further the already rich *P*-*T* phase diagrams of A_2B_3 compounds.

The transition into the bcc phase is not fully completed at 65 GPa for Sb_2Se_3, the highest pressure reached in this study, as some remnant *Pnma* phase can still be observed in the XRD patterns [**Fig. 2(b)**]. The fitting of the *P*-*V* data for the bcc phase with a Birch-Murnaghan EOS form [**Fig. 3(b)**] yields the following values for the elastic parameters: $V_{Tr}/Z = 87.25(\pm 0.1)$ Å^3 and $B_{Tr} = 217(\pm 11)$ GPa, with $B'_{Tr} = 4$ (fixed value) and $Z = 0.4$[19]. It should be also noted here that the *P*-*V* data employed for the bcc EOS fitting correspond to both compression [filled symbols in **Fig. 3(b)**] and decompression [open symbols in **Fig. 3(b)**] cycles. Therefore, the transition pressure point P_{Tr} for the *Pnma*-*Im*-3*m* transition, where the obtained elastic parameters are evaluated, is assumed to occur at 36.2 GPa for the EOS fitting purposes.

In addition, we have probed the high-pressure vibrational features of Sb_2Se_3 by employing Raman spectroscopy. For the starting *Pnma* phase, a sum of thirty first-order Raman-active modes are expected[33]:

$$\Gamma = 10A_g + 5B_{1g} + 10B_{2g} + 5B_{3g} \quad (1)$$

At ambient conditions [bottom spectra in **Fig. 4(a)**], the Raman spectrum of Sb_2Se_3 consists of eight relatively sharp peaks (labeled 1–8) and some broad Raman features, such as the low-intensity "wings" of peak 3. Upon pressure application, these broad bands become more prominent and can be clearly resolved (D1–D3, **Fig. 4**). Given the distinct width differences between the sharp and broad Raman features in the Sb_2Se_3 Raman spectra, we speculate that the scattering mechanism and, therefore, the origin of these Raman bands are different. We assign the sharp Raman features to first-order Raman-active modes of Sb_2Se_3 (except for mode 8), whereas the broad bands to defect-induced Raman scattering. Our arguments are the following:

(a) Structural defects are known to affect the Raman response of crystalline materials, by introducing broad bands in the measured Raman spectra[34,35]. This kind of defect-induced Raman scattering mechanism has been explored in detail for several binary semiconductors[34].

(b) Most of the reported ambient-pressure Sb_2Se_3 Raman spectra exhibit only sharp Raman features[36–38], which are consistent with our observed (1–7) Raman peaks. In addition, additional TEM measurements performed on these Sb_2Se_3 materials[36–38] established their high crystalline quality. On the other hand, the Raman spectra of Sb_2Se_3 reported in Refs. 29, 39 are quite different. The main feature in both of these studies is a broad Raman band located at ~190 cm^{-1}; since no other microstructural studies were provided in those investigations, the crystalline quality of the measured samples is unclear and questionable. Nevertheless, this apparent discrepancy prompted us to conduct additional Raman measurements on Sb_2Se_3 (see Supplementary Information).

(c) As part of these detailed Raman investigations, we have studied the effect of laser annealing on the Raman response of Sb_2Se_3 at ambient pressure. After the laser annealing process, the background in the Sb_2Se_3 Raman spectrum becomes completely flat, whereas the broad features are eliminated completely [see Supplementary **Fig. S6(a)** online]. Given that such laser-annealing/high-temperature treatment induces analogous effects, i.e. improves the quality of the 3C-SiC Raman spectra due to the suppression of microstructural disorder[40], we can

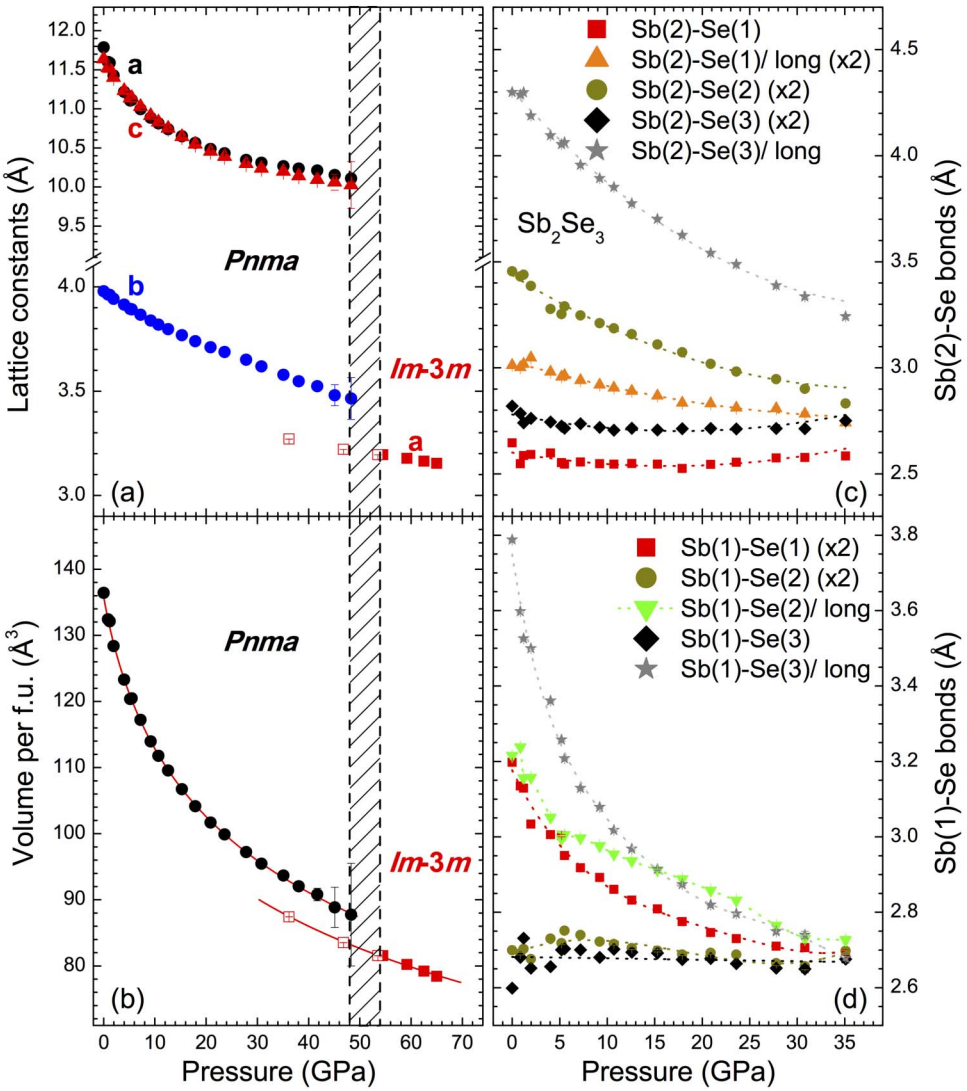

Figure 3 | (a) Lattice constants and (b) unit cell volume per formula unit as a function of pressure for the two phases of Sb_2Se_3. The closed and open symbols correspond to data collected upon compression and decompression cycles, respectively. The dashed rectangle marks the transition regime for the *Pnma-Im-3m* structural transition. The red solid lines represent the fitted Birch-Murnaghan EOS functions to the measured *P-V* data. (c, d) Pressure-induced changes of the Sb(2)-Se and the Sb(1)-Se bond lengths within the $Sb(2)Se_{7+1}$ and $Sb(1)Se_7$ polyhedra, respectively, for the *Pnma* phase of Sb_2Se_3. The various Sb-Se bond distances are displayed in **Fig. 1** for clarity.

Table 1 | Refined crystallographic data for the starting *Pnma* structure and the high-pressure *Im-3m* modification of Sb_2Se_3 [Fig. 2(b)]

Space Group	*Pnma* (62)	*Im-3m* (229)
Pressure (GPa)	9.2	65
a (Å)	10.8837(1)	3.1538(2)
b (Å)	3.8378(1)	3.1538(2)
c (Å)	10.9118(1)	3.1538(2)
c/a	1.003	1
c/b	2.843	1
a/b	2.836	1
V (Å^3)	455.8	31.4
Z	4	2
wR_p, $R(F^2)$	0.017, 0.124	0.038, 0.245
Atomic coordinates	Sb(1): 4c [−0.00291(1), 0.25, 0.67724(3)] Sb(2): 4c [0.3432(1), 0.25, 0.4559(2)] Se(1): 4c [0.05968(2), 0.25, 0.13273(3)] Se(2): 4c [0.36755(3), 0.25, 0.06293(2)] Se(3): 4c [0.21616(2), 0.25, 0.78949(3)]	Sb/Se: 2a (0, 0, 0)

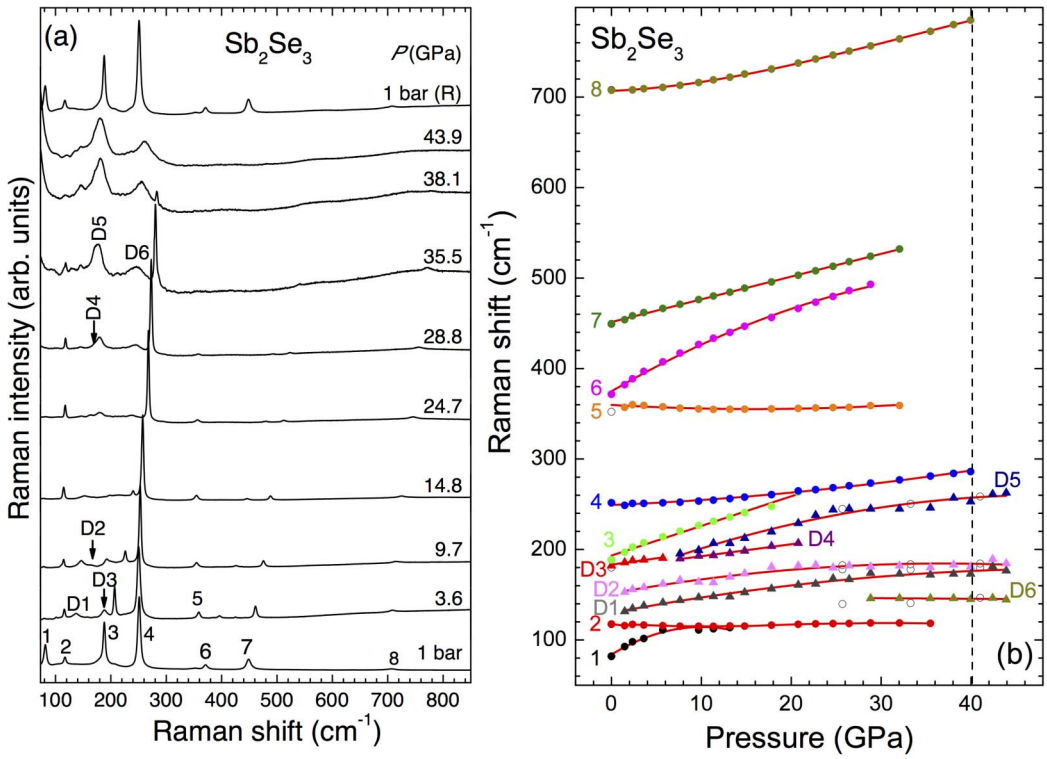

Figure 4 | (a) Raman spectra of Sb_2Se_3 at various pressures ($\lambda = 532$ nm, $T = 300$ K). (b) Raman mode frequency evolution against pressure. Solid circles and triangles correspond to crystalline and disorder-induced Raman features of Sb_2Se_3, respectively (see text). The open symbols correspond to data collected upon decompression. Solid lines represent least square fits to the measured data. The vertical dashed line denotes the loss of the sharp Raman features in the Sb_2Se_3 Raman spectra.

reasonably assume that a similar effect is taking place in the case of Sb_2Se_3 as well.

The measured zero-pressure frequencies ω_0 for the first-order Raman modes of Sb_2Se_3 (Supplementary **Table S1** online) are in good agreement with the reported values[36–38]. The Raman mode assignment (1–7) is achieved by comparing the (almost identical) Raman spectra of isostructural Sb_2Se_3 and Sb_2S_3 compounds (see Supplementary **Fig. S7** online). All of the observed sharp Raman peaks (1–7) are thus identified as first-order Raman modes. The only notable exception is mode 8 located at ~705 cm^{-1}; interestingly, this mode is present in both Sb_2Se_3 and Sb_2S_3 compounds, as well as in the cubic Sb_2O_3 (see Supplementary **Fig. S7** online). Although such mode is expected in the case of Sb_2O_3 due to the presence of the light oxygen anion[41], it is not anticipated for the heavier S- and Se-bearing compounds. By taking also into account its (almost) identical pressure dependence with the respective F_{2g} mode of Sb_2O_3[41], we attribute mode 8 to an impurity Raman band.

Upon compression, most of the first-order Raman-active modes of Sb_2Se_3 (1–7) exhibit "normal" behavior, i.e. their frequencies shift to higher values with increasing pressure (**Fig. 4**). The effect of pressure is more pronounced for the 1, 3, 6, and 7 Raman modes, implying that the respective force constants are more sensitive against pressure application. This larger pressure dependence results in the merging of both 1 and 3 modes with their neighboring 2 and 4 bands above 10 and 20 GPa, respectively. On the contrary, mode 5 exhibits pressure-induced softening (even though marginal) up to 32 GPa. Since this mode is assigned to a Sb-Se stretching motion, it most likely reflects the pressure-induced behavior of the shorter (and almost incompressible) Sb-Se bonds [**Figs. 3 (c, d)**].

As for the disorder-induced D1, D2, and D3 modes, their frequencies increase with increasing pressure. Mode D3 broadens significantly above 7.5 GPa; two bands (D4 and D5 in **Fig. 4**) are employed for the fitting of this feature beyond this pressure point. Upon further compression, an additional broad band (D6) appears in our Raman spectra above 29 GPa. Coincidentally, the strongest sharp peak of Sb_2Se_3 (mode 4) starts to decline in intensity, whereas the broad Raman features (D1, D3, and D5) enhance above that pressure intensity-wise. Mode 4 can be resolved up to 40 GPa; the Raman spectra are dominated by the four D1, D3, D5, and D6 broad bands beyond that pressure (**Fig. 4**).

The total loss of the sharp Raman peaks above 40 GPa coincides roughly with the broadening of the Bragg peaks evidenced in the XRD patterns (**Fig. 2**). Since the *Pnma-Im-3m* structural transition initiates at a higher pressure, i.e. above 51 GPa, the loss of the sharp peaks in the Raman spectra arises probably due to pressure-induced structural disorder rather than a structural transition. However, and since the high-pressure *Im-3m* structure is both a disordered and a Raman-inactive phase, this utter loss of the sharp Raman features above 40 GPa might also be a signature for the *Pnma-Im-3m* structural transition. The original phase/Raman spectrum of Sb_2Se_3 is recovered upon decompression (**Fig. 4**), but only after full pressure release.

Before finishing this Section, a direct comparison between our high-pressure Raman study and that of Bera *et al.*[29] is in order. As mentioned before, our Sb_2Se_3 Raman spectra are quite different from those reported in Ref. 29, where the main feature of the Raman spectra is a broad band located at ~190 cm^{-1}. In order to resolve this discrepancy, we have probed the Raman activity of Sb_2Se_3 in different environments and experimental conditions [see Supplemental **Fig. S6(b)** online]. In particular, the form of the sample (single-crystalline or grounded powder) does not influence the Raman response at ambient conditions. On the contrary, the choice of the pressure transmitting medium (PTM) employed for the high-pressure measurements affects the Raman signal of Sb_2Se_3 significantly. More precisely, the Raman spectrum of Sb_2Se_3 measured with

helium as PTM (the PTM employed for this study) is consistent with the Raman spectra obtained from the sample at ambient conditions. Employing mixtures of methanol-ethanol-water (M/E/W) 16 : 3 : 1 and methanol-ethanol (M/E) 4 : 1 as PTM, however, alters the Raman response of Sb_2Se_3 drastically: the strongest Raman band is now located at ~190 cm^{-1}, whereas the intense Raman peak at ~250 cm^{-1} is absent from the Raman spectra in both cases. The Raman spectra obtained in this case resemble that of Ref. 29. It should be noted, however, that the Raman spectra obtained with M/E/W and M/E exhibit also distinct differences between each other, e.g. completely different relative intensities of the Raman peaks [Supplemental **Fig. S6(b)** online]. Therefore, it becomes clear that the choice of PTM affects the Raman response of Sb_2Se_3. Since the Raman response of Sb_2Se_3 at ambient conditions matches that of Sb_2Se_3 embedded in the helium PTM [Supplemental **Fig. S6(b)** online], we are confident that helium is the proper PTM for conducting high-pressure Raman investigations. In the case of the alcohol mixtures on the other hand, the different Raman spectra imply a possible reaction between the material and the PTM.

Discussion

As mentioned before, the series of A_2B_3 (A = Sb, Bi; B = S, Se, Te) compounds can be structurally divided into two classes: the heavier Sb_2Te_3, Bi_2Te_3, and Bi_2Se_3 materials adopt a rhombohedral *R*-3*m* structure at ambient conditions, with sixfold coordination around the A cations. On the other hand, the lighter Sb_2Se_3, Sb_2S_3, and Bi_2S_3 systems crystallize in the denser *Pnma* phase with mixed cationic coordinations (sevenfold and eightfold).

Regarding the former, recent high-pressure studies of the Bi_2Te_3[6–13], Bi_2Se_3[14–18], and Sb_2Te_3[9,19–23] compounds have revealed several interesting effects. In particular, a pressure-induced electronic topological transition has been observed for all of these materials in the *R*-3*m* phase[10,11,18,22]. This feature has been associated with an enhancement of their thermoelectric properties under pressure[1,42,43]. In addition, pressure-induced superconductivity has been reported for both Bi_2Te_3[12,13] and Sb_2Te_3[23] systems.

Regarding the reported structural transitions, all Bi_2Te_3[6–13], Bi_2Se_3[14–18], and Sb_2Te_3[9,19–23] compounds adopt a monoclinic phase (SG *C*2/*m*, *Z* = 4) above 10 GPa, accompanied by changes in their electronic properties. In this structure, the coordination of the A cations increases to sevenfold with respect to the chalcogenide anions. Upon further pressure increase, the structural evolution varies: both Bi_2Te_3[6] and Sb_2Te_3[20] compounds adopt another monoclinic structure (SG *C*2/*c*, *Z* = 4) with eightfold coordination at ~13 GPa, whereas a disordered bcc phase (SG *Im*-3*m*, *Z* = 2) appears above 15 GPa and 22 GPa, respectively. In addition, an intermediate bcc-like monoclinic phase (*C*2/*m*) has been reported for Sb_2Te_3[19]. These structural transitions are reversible upon pressure release.

Regarding the pressure-induced structural behavior of Bi_2Se_3, however, things are more complex: in Ref. 15, Bi_2Se_3 was shown to transform from the first high-pressure *C*2/*m* phase directly into a body-centered tetragonal structure (SG *I*4/*mmm*, *Z* = 2) above 25 GPa[15]; upon decompression, an amorphous phase is recovered. Given sufficient relaxation time, the orthorhombic Bi_2Se_3-II phase (isostructural to Sb_2Se_3), forms from the amorphous material[15]. This phase has been observed before under combined high-pressure and high-temperature conditions[24]. Regarding the stability of Bi_2Se_3-II under pressure, the orthorhombic *Pnma* phase was reported to persist up to 26 GPa[15]. In Ref. 14 on the other hand, Bi_2Se_3 is found to exhibit the same structural sequence as the Bi_2Te_3 and Sb_2Te_3 materials, i.e. *R*-3*m*- > *C*2/*m*- > *C*2/*c*. Upon further compression, however, instead of a disordered bcc phase, a novel monoclinic phase (SG *C*2/*m*, *Z* = 4) was observed. In this structure, the Bi cations adopt a mixed ninefold and tenfold coordination with respect to the Se anions. The absence of the high-pressure bcc phase was attributed to the large ionic radii difference between the Bi and Se ions. Given this structural diversity in the high-pressure behavior of Bi_2Se_3, it appears that the choice of PTM (M/E and Si oil in Ref. 15, M/E in Ref. 14), as well as the sample quality (as-synthesized in Ref. 15, commercial in Ref. 14) may significantly influence the structural evolution of these materials under pressure. Even though a plethora of results is available, it certainly appears that more systematic high-pressure structural investigations are needed in order to establish the connection between the structural evolution of these A_2B_3 materials and the experimental parameters.

Turning now to the material at hand, the disordered high-pressure *Im*-3*m* phase of Sb_2Se_3 represents a novel binary structure/alloy between Sb and Se atoms; the only known binary crystalline phase between Sb and Se is the *Pnma* structure with A_2B_3 composition. The formation mechanism of the bcc alloy is not easy to understand intuitively, since the atomic radii of Sb and Se atoms (r_{Sb} = 1.33 Å, r_{Se} = 1.03 Å) are quite different at ambient pressure. A plausible explanation may be that charge transfer from the Sb cations towards the Se anions is taking place under pressure, thus "equalizing" the two ionic radii and favoring the disordered structure, as in Bi_2Te_3[6]. Such pressure-induced charge transfer is probably correlated with the gradual suppression of the Sb^{3+} lone electron pair stereochemical activity in the *Pnma* phase [see Supplementary **Fig. S6(b)** online].

Given the disordered nature of the high-pressure Bi_2Te_3, Sb_2Te_3, and Sb_2Se_3 bcc phases, we speculate that these modifications will most likely transform into ordered crystalline structures upon sufficient heating (unless decomposition occurs). A plausible structural candidate after such high-temperature treatment might be the defect cubic Th_3P_4-type phase (SG *I*-43*d*, *Z* = 4), with eightfold cationic coordination. This structure is a common polymorph for rare-earth based A_2B_3 chalcogenides (γ-phase) at high-temperature and/or high-pressure conditions[44]. Furthermore, this cubic modification is structurally resilient against pressure increase[45]. The disordered high-pressure bcc modifications of the heavier Bi_2Te_3 and Sb_2Te_3 compounds are more suitable candidates for testing this suggestion, mainly due to their lower transition pressures.

Finally, we would like to add some thoughts on the electronic properties of Sb_2Se_3 in the high-pressure bcc modification. At ambient conditions, Sb_2Se_3 is an insulator with a band gap of ~1 eV[25]. Given that (a) the high-pressure bcc phases of both Bi_2Te_3[6,13] and Sb_2Te_3[23] are metallic and superconducting and (b) the respective high-pressure CsCl-type/bcc modifications for several binary compounds are also metallic[46] and even superconducting[47], it is reasonable to assume that the high-pressure bcc phase of Sb_2Se_3 will also exhibit metallic, and possibly superconducting behavior. This assumption, however, needs to be checked by appropriate high-pressure electrical transport measurements.

Methods

Sample and high-pressure technique details. The Sb_2Se_3 compound was available in single-crystalline form (Alfa-Aesar, 99.999% purity). Both the XRD and TEM measurements at ambient conditions did not detect any impurity phases. For the x-ray measurements, the single crystals were grinded into fine powder.

Pressure was generated by a symmetric diamond anvil cell (DAC) with 300 μm diamond culet diameter. A 150 μm diameter hole was drilled in the middle of a preindented rhenium gasket of 40 μm thickness and served as the sample chamber. Liquid helium was employed as a PTM for both high-pressure x-ray diffraction (XRD) and Raman investigations. The helium loading took place at the gas-loading facility of GeoSoilEnviroCARS/Sector 13[48], located at the Advanced Photon Source (APS) of Argonne National Laboratory (ANL). The ruby luminescence method was employed for pressure measurement[49].

Angle-dispersive powder x-ray diffraction. The monochromatic angle-dispersive powder XRD measurements under pressure were performed at the 16BM-D beamline of the High Pressure Collaborative Access Team, at APS-ANL. The x-ray beam size was ~8 μm × 12 μm and the x-ray wavelength was λ = 0.4246 Å. The XRD patterns were collected with a MAR 345 Image Plate detector. The intensity. vs. 2θ patterns were obtained using the FIT2D software[50]. Refinements of the measured XRD patterns were performed using the GSAS + EXPGUI software packages[51,52]. The measured *P*-*V* data for both the ambient-pressure *Pnma* and high-pressure *Im*-3*m* phases were fitted with a Birch-Murnaghan equation of state (EOS)[53]. Crystal-

chemical calculations were performed with the IVTON software[54]. We should emphasize here that there exist several available settings for SG *Pnma*; here we choose to employ the same *Pnma* setting as in isostructural Sb_2S_3[31] and Bi_2S_3[32] compounds.

Transmission electron microscopy. In order to verify the reversibility of the original phase of Sb_2Se_3 from the XRD study, we have performed transmission electron microscopy (TEM) studies on the starting Sb_2Se_3 sample (crushed powder) and the quenched Sb_2Se_3 powder, i.e. the Sb_2Se_3 sample recovered after full decompression from the aforementioned XRD study. For this purpose, the samples were dispersed onto holey-carbon TEM grids and were analyzed using a JEOL 3011 microscope by means of high-resolution TEM images (HRTEM) and selected area electron diffraction (SAED) patterns.

High-pressure Raman spectroscopy. The high-pressure Raman experiments were conducted on single-crystalline Sb_2Se_3 samples with a solid-state laser ($\lambda = 532$ nm) coupled to a single-stage Raman spectrometer (Andor S500i) and a charge-coupled device. The spectral resolution was 2 cm^{-1} and the lowest resolvable frequency was ~75 cm^{-1}. The size of the laser spot on the sample surface was approximately 30 μm, whereas the laser power was 2 mW outside the DAC (unless specified otherwise). In order to investigate the effect of PTM, as well as the effect of the incident laser power on the sample, additional Raman measurements on Sb_2Se_3 were conducted. These extra Raman studies are presented in the Supporting Information (SI).

1. Ovsyannikov, S. V. & Shchennikov, V. V. High-Pressure Routes in the Thermoelectricity or How One Can Improve a Performance of Thermoelectrics. *Chem. Mater.* **22**, 635 (2010).
2. Chen, Y. L. *et al.* Experimental Realization of a Three-Dimensional Topological Insulator, Bi_2Te_3. *Science* **325**, 178 (2009).
3. Zhang, H. J. *et al.* Topological insulators in Bi_2Se_3, Bi_2Te_3 and Sb_2Te_3 with a single Dirac cone on the surface. *Nat. Phys.* **5**, 438 (2009).
4. Qi, X.-L. & Zhang, S.-C. Topological insulators and superconductors. *Rev. Mod. Phys.* **83**, 1057 (2011).
5. Yan, B. & Zhang, S.-C. Topological materials. *Rep. Prog. Phys.* **75**, 96501 (2012).
6. Zhu, L. *et al.* Substitutional Alloy of Bi and Te at High Pressure. *Phys. Rev. Lett.* **106**, 145501 (2011).
7. Einaga, M. *et al.* Pressure-induced phase transition of Bi_2Te_3 to a bcc structure. *Phys. Rev. B* **83**, 92102 (2011).
8. Einaga, M., Tanabe, Y., Ohmura, A. N. A., Ishikawa, F. & Yamada, Y. New superconducting phase of Bi_2Te_3 under pressure above 11 GPa. *J. Phys.: Conf. Ser.* **215**, 12036 (2010).
9. Jacobsen, M. K., Sinogeikin, S. V., Kumar, R. S. & Cornelius, A. L. High pressure transport characteristics of Bi_2Te_3, Sb_2Te_3, and $BiSbTe_3$. *J. Phys. Chem. Sol.* **73**, 1154 (2012).
10. Pradhan, G. K., Bera, A., Kumar, P., Muthu, D. V. S. & Sood, A. K. Raman signatures of pressure induced electronic topological and structural transitions in Bi_2Te_3. *Sol. St. Comm.* **152**, 284 (2012).
11. Vilaplana, R. *et al.* High-pressure vibrational and optical study of Bi_2Te_3. *Phys. Rev. B* **84**, 104112 (2011).
12. Zhang, J. L. *et al.* Pressure-induced superconductivity in topological parent compound Bi_2Te_3. *PNAS* **108**, 24 (2011).
13. Zhang, S. J. *et al.* The comprehensive phase evolution for Bi_2Te_3 topological compound as function of pressure. *J. Appl. Phys.* **111**, 112630 (2012).
14. Liu, G. T., Zhu, L., Ma, Y. M., Lin, C. L. & Liu, J. Stabilization of 9/10-Fold Structure in Bismuth Selenide at High Pressures. *J. Phys. Chem. C* **117**, 10045 (2013).
15. Zhao, J. *et al.* High-pressure phase transitions, amorphization, and crystallization behaviors in Bi_2Se_3. *J. Phys. Cond. Matt.* **25**, 125602 (2013).
16. Hamlin, J. J. *et al.* High pressure transport properties of the topological insulator Bi_2Se_3. *J. Phys. Cond. Matt.* **24**, 35602 (2012).
17. Segura, A. *et al.* Trapping of three-dimensional electrons and transition to two-dimensional transport in the three-dimensional topological insulator Bi_2Se_3 under high pressure. *Phys. Rev. B* **85**, 195139 (2012).
18. Vilaplana, R. *et al.* Structural and vibrational study of Bi_2Se_3 under high pressure. *Phys. Rev. B* **84**, 184110 (2011).
19. Zhao, J. *et al.* Pressure-Induced Disordered Substitution Alloy in Sb_2Te_3. *Inorg. Chem.* **50**, 11291 (2011).
20. Ma, Y. *et al.* Determinations of the high-pressure crystal structures of Sb_2Te_3. *J. Phys.: Cond. Matter* **24**, 475403 (2012).
21. Souza, S. M. *et al.* High pressure monoclinic phases of Sb_2Te_3. *Phys. B* **407**, 3781 (2012).
22. Gomis, O. *et al.* Lattice dynamics of Sb_2Te_3 at high pressures. *Phys. Rev. B* **84**, 174305 (2011).
23. Zhu, J. *et al.* Superconductivity in Topological Insulator Sb_2Te_3 Induced by Pressure. *Sci. Rep.* **3**, 2016 (2013).
24. Atabaeva, E. Y., Mashkov, S. A. & Popova, S. V. Die Kristallstruktur der neuen Modifikation von Bi2 Se3 II. *Kristallogr.* **18**, 173 (1973).
25. Koc, H., Mamedov, A. M., Deligoz, E. & Ozisik, H. First principles prediction of the elastic, electronic, and optical properties of Sb_2S_3 and Sb_2Se_3 compounds. *Sol. St. Sci.* **14**, 1211 (2012).
26. Arun, P., Vedeshwar, A. G. & Mehra, N. C. Laser-induced crystallization in amorphous films of Sb_2C_3 (C = S, Se, Te), potential optical storage media. *J. Phys. D: Appl. Phys.* **32**, 183 (1999).
27. Fernandez, A. M. & Merino, M. G. Preparation and characterization of Sb_2Se_3 thin films prepared by electrodeposition for photovoltaic applications. *Th. Sol. Films* **366**, 202 (2000).
28. Minnich, A. J., Dresselhaus, M. S., Ren, Z. F. & Chen, G. Bulk nanostructured thermoelectric materials: current research and future prospects. *Energy Environ. Sci.* **2**, 466 (2009).
29. Bera, A. *et al.* Sharp Raman anomalies and broken adiabaticity at a pressure induced transition from band to topological insulator in Sb_2Se_3. *Phys. Rev. Lett.* (2013).
30. Liu, W. *et al.* Anisotropic interactions and strain-induced topological phase transition in Sb_2Se_3 and Bi_2Se_3. *Phys. Rev. B* **84**, 245105 (2011).
31. Lundegaard, L. F., Miletich, R., Balic-Zunic, T. & Makovicky, E. Equation of state and crystal structure of Sb_2S_3 between 0 and 10 GPa. *Phys Chem Miner.* **30**, 463 (2003).
32. Lundegaard, L. F., Makovicky, E., Boffa-Ballaran, T. & Balic-Zunic, T. Crystal structure and cation lone electron pair activity of Bi_2S_3 between 0 and 10 GPa. *Phys Chem Miner.* **32**, 578 (2005).
33. Sereni, P., Musso, M., Knoll, P., amd, K., Schwarz, P. B. & Schmidt, G. Polarization-Dependent Raman Characterization of Stibnite (Sb_2S_3). *AIP Conf. Proc.* **1267**, 1131 (2010).
34. Falkovsky, L. A. Investigation of semiconductors with defects using Raman scattering. *Phys. Usp.* **47**, 249 (2004).
35. Wieligor, M., Wang, Y. & Zerda, T. W. Raman spectra of silicon carbide small particles and nanowires. *J. Phys. Cond. Matt.* **17**, 2387 (2005).
36. Ma, X. *et al.* Large-scale growth of wire-like Sb_2Se_3 microcrystallines via PEG-400 polymer chain-assisted route. *J. Cryst. Growth* **263**, 491 (2004).
37. Wang, J., Deng, Z. & Li, Y. Synthesis and characterization of Sb_2Se_3 nanorods. *Mater. Res. Bull.* **37**, 495 (2002).
38. Zhai, T. *et al.* Single-Crystalline Sb_2Se_3 Nanowires for High-Performance Field Emitters and Photodetectors. *Adv. Mater.* **22**, 4530 (2010).
39. Ivanova, Z. G., Cernoskova, E., Vassilev, V. S. & Boycheva, S. V. Thermomechanical and structural characterization of $GeSe_2$-Sb_2Se_3-ZnSe glasses. *Mater. Lett.* **57**, 1025 (2003).
40. Rohmfeld, S., Hundhausen, M. & Ley, L. Influence of Stacking Disorder on the Raman Spectrum of 3C-SiC. *Phys. Stat. Sol. (b)* **215**, 115 (1999).
41. Pereira, A. L. J. *et al.* Structural and vibrational study of cubic Sb_2O_3 under high pressure. *Phys. Rev. B* **85**, 174108 (2012).
42. Ovsyannikov, S. V. *et al.* Giant improvement of thermoelectric power factor of Bi_2Te_3 under pressure. *J. Appl. Phys.* **104**, 53713 (2008).
43. Ovsyannikov, S. V. *et al.* Thermoelectric properties of p-Bi2−xSb Te-x(3) solid solutions under pressure. *Phys. Sol. St.* **54**, 261 (2012).
44. Grzechnik, A. Lanthanide polysulfides at high pressures. *J. All. Comp.* **317**, 190 (2001).
45. Grzechnik, A. Stability and Optical Properties of c-Gd_2S_3 at High Pressures. *J. Sol. St. Chem.* **148**, 370 (1999).
46. Ovsyannikov, S. V. *et al.* Unusual B1-B2 transition in PbSe under high pressure: evidence for two intermediate phases; transport, structural, and optical properties. *Phys. Stat. Sol. b* **246**, 615 (2009).
47. Timofeev, Y. A., Vinogradov, B. V. & Begoulev, V. B. Superconductivity of tin selenide at pressures up to 70 GPa. *Phys. Sol. St.* **39**, 236 (1997).
48. Rivers, M., Prakapenka, V. B., Kubo, A., Pullins, C. & Jacobsen, C. M. H. S. D. The COMPRES/GSECARS gas-loading system for diamond anvil cells at the Advanced Photon Source. *High Press. Res.* **28**, 273 (2008).
49. Mao, H. K., Xu, J. & Bell, P. Calibration of the Ruby Pressure Gauge to 800 kbar Under Quasi-Hydrostatic Conditions. *J. Geophys. Res.* **91**, 4673 (1986).
50. Hammersley, A. P., Svensson, S. O., Hanfland, M., Fitch, A. N. & Hausermann, D. Two-dimensional detector software: From real detector to idealised image or two-theta scan. *High Pres. Res.* **14**, 235 (1996).
51. Von Dreele, R. B. & Larson, A. C. GSAS. *Los Alamos National Laboratory Report No. LAUR 86–748* (1994).
52. Toby, B. H. EXPGUI, a graphical user interface for GSAS. *J. Appl. Crystallogr.* **34**, 210 (2001).
53. Birch, F. Finite Elastic Strain of Cubic Crystals. *Phys. Rev.* **71**, 809 (1947).
54. Zunic, T. B. & Vickovic, I. IVTON - a program for the calculation of geometrical aspects of crystal structures and some crystal chemical applications. *J. Appl. Crystallogr.* **29**, 305 (1996).

Acknowledgements

Portions of this work were performed at HPCAT (Sector 16), Advanced Photon Source (APS), Argonne National Laboratory. HPCAT operations are supported by DOE-NNSA under Award No. DE-NA0001974 and DOE-BES under Award No. DE-FG02-99ER45775, with partial instrumentation funding by NSF. APS is supported by DOE-BES, under Contract No. DE-AC02-06CH11357. The compressed helium gas loading was performed at GeoSoilEnviroCARS (Sector 13), APS-ANL. GeoSoilEnviroCARS is supported by the National Science Foundation-Earth Sciences (EAR-0622171) and Department of Energy-Geosciences (DE-FG02-94ER14466). We would like to acknowledge Dr. S. Tkachev for his help with the DAC gas loading at GSECARS, as well as Dr. D. Ikuta with his

assistance during the XRD measurements. We are grateful to Prof. A. K. Sood for providing the manuscript of Ref. 29 prior to publication, and Dr. A. L. J. Pereira for the ambient-conditions XRD and Raman data of Sb_2O_3. Finally, we would like to thank Prof. Balic-Zunic Momma for providing the IVTON software.

Author contributions

I.E. and Y.W. conceived and designed the research, I.E., M.K., C.P. and Y.W. conducted the high pressure experiments, J.Z. carried out the TEM measurements and provided the related images and text, I.E. and Y.W. wrote the manuscript, R.E. revised and commented the manuscript.

Additional information

Supplementary information accompanies this paper at http://www.nature.com/scientificreports

Competing financial interests: The authors declare no competing financial interests.

How to cite this article: Efthimiopoulos, I. *et al.* Sb_2Se_3 under pressure. *Sci. Rep.* **3**, 2665; DOI:10.1038/srep02665 (2013).

This work is licensed under a Creative Commons Attribution-NonCommercial-NoDerivs 3.0 Unported license. To view a copy of this license, visit http://creativecommons.org/licenses/by-nc-nd/3.0